

# Trifunctional local-range order oxygen structure enhanced strength-ductility and fatigue resistance in large-scale metastable titanium alloy

Received: 13 December 2024

Accepted: 24 July 2025

Published online: 04 August 2025

 Check for updates

Yamei Mao<sup>1</sup>, Qinyang Zhao<sup>1</sup>✉, Runqi Zhang<sup>2,3</sup>, Ping Guo<sup>3</sup>,  
Yongnan Chen<sup>1</sup>✉ & Yongqing Zhao<sup>1,3</sup>

Research on high-performance Ti alloys incorporating oxygen (O) has remained a laboratory procedure and is hindered by the unresolved issue of O segregation-driven failure. Here, we demonstrate that O can tailor a nanoscale local range order O (LRO-O) structure between the oxide and random interstitials in Ti alloy. We introduce 0.36 wt% O into metastable Ti-5Al-5Mo-5V-3Cr alloy using a short-term powder metallurgy approach to produce large-scale materials. The LRO-O structure in designed alloy prevents crack initiation by promoting the active nucleation of <c>-type dislocations and altering the slip modes during tensile and fatigue failure. The alloy has high strength (1.7 GPa), elongation (7.9%), and fatigue strength (1058.3 MPa), which outperforms many high-strength, high-O Ti alloys. Our findings provide a scalable, practical route to superior mechanical properties for Ti alloys without costly alloying elements.

Driven by the goals of lightweight design in aerospace applications, solving the inherent trade-off dilemma between strength and ductility, along with the ambiguous relationship between fatigue strength and strength-ductility, has been a significant challenge in the attainment of high-performance titanium (Ti) alloys<sup>1–4</sup>. Optimizing the composition and microstructure using thermomechanical processing and heat treatment is a key strategy for enhancing the synergy between strength and ductility<sup>5–7</sup>. Despite these advances, challenges remain in achieving higher yield strength and improving fatigue resistance.

The controlled addition of interstitial oxygen (O) has emerged as a transformative strategy for enhancing the mechanical properties of Ti alloys. Interstitial O enhances the strength of Ti alloys not only through interstitial solid solution strengthening, but also by influencing the formation and stability of metastable phases ( $\omega$ ,  $\alpha'$ , and  $\alpha''$  etc.)<sup>8,9</sup>. In addition, O uniquely refines microstructures, intensifies the dislocation activity, activates the double-slip and <c + a>-type dislocations,

and influences the twinning modes<sup>9–20</sup>. Due to these attributes, O is indispensable for developing high-performance Ti alloys<sup>9–20</sup>. Controlled O addition improves yield strength and some Ti alloys have been reported to retain reasonable ductility<sup>17,21–24</sup>, but keeping intermediate ductility at high strength level is still difficult<sup>25,26</sup>. Additionally, studies on the fatigue resistance of high O content Ti alloys are limited because of a severe decline in fatigue life at high O levels<sup>26,27</sup>. These adverse effects result from crack initiation and propagation by O-induced due to O segregation and localized plastic deformation, such as grain boundary cracking,  $\alpha$  phase cleavage and shearing, and  $\alpha/\beta$  interface debonding<sup>26,28</sup>. These shortcomings, compounded by processing complexities, confine high O content Ti alloys to the laboratory stage<sup>29–33</sup>. Therefore, resolving O segregation is pivotal for industrializing high-strength and ductile Ti alloys with high O content and revealing their potential for aerospace and other demanding applications.

<sup>1</sup>School of Materials Science and Engineering, Chang'an University, Xi'an, People's Republic of China. <sup>2</sup>School of Materials Science and Engineering, Northeastern University, Shenyang, People's Republic of China. <sup>3</sup>Northwest Institute for Non-ferrous Metal Research, Xi'an, People's Republic of China.

✉ e-mail: [zqy@chd.edu.cn](mailto:zqy@chd.edu.cn); [frank\\_cyn@163.com](mailto:frank_cyn@163.com)

The chemical local range order (LRO) structures, which contain chemical short/medium-range order (SRO/MRO) structures, can coordinate deformation by changing the dislocation shear mode, thereby fostering work hardening and enhancing the fatigue resistance of metallic materials<sup>34–36</sup>. Our work introduces 0.36 wt% O into the widely used Ti-5Al-5Mo-5V-3Cr (Ti-5553) commercial metastable Ti alloy prepared via a powder metallurgy short process (vacuum sintering, conventional forging, bar rolling, and one-step low-temperature annealing) to obtain large-scale materials (lengths above 6 m with a diameter of 16 mm). Thus, these materials have great industrialization potential. Besides, as the control sample, the 0.22 wt% O was introduced into Ti-5553 alloy using the same method.

Here, the interstitial O atoms were tailored to a local range order (LRO-O) structure in Ti-5553-0.36 O alloy, which is designed to reduce and even eliminate O segregation and inhibit crack nucleation at interfaces. This structure achieves a trifunctional synergy of strength, ductility, and fatigue strength by promoting the formation of <c>-type dislocations, enabling cross-slip, shifting the slip from planar to wavy for plastic flow homogenization under tensile deformation, and combining <c>-type dislocation interactions with twinning and dominant planar slip to enhance fatigue resistance. This research provides an approach that directly enhances the design of alloys with comprehensive high-performance and can be readily scaled up for the application of large complex structural components; thus, critical insights are provided for future developments in metal materials.

## Results and discussion

### Microstructure and inner LRO-O structure

We designed two Ti-5553-xO alloys with different O contents (0.22 wt% and 0.36 wt%), which will be referred to as the 0.22 O alloy and 0.36 O alloy in the following part of this study. The 0.22 O alloy exhibits a macroscopically uniform microstructure, characterized by a continuous distribution of the primary  $\alpha$  ( $\alpha_p$ ) phase and a regional distribution of the secondary  $\alpha$  ( $\alpha_s$ ) phase with varying sizes at the microscale (Supplementary Fig. 1a–c). The LRO-O structures have not been detected in 0.22 O alloy (Supplementary Fig. 1d–f). Thus, due to the page limitation, we mainly focus on the 0.36 O alloy, to illustrate the effects of LRO-O structures. The microstructure of the 0.36 O alloy exhibited a distinct layered structure, characterized by a pronounced chain-like morphology of the  $\alpha_p$  phase and a disordered distribution of the  $\alpha_s$  phase within the  $\beta$  grains (Fig. 1a and Supplementary Fig. 1g–i). Moreover, the size difference of the  $\alpha_s$  phase varies due to thermo-mechanical processing and annealing. The three-dimensional reconstructions of the alloys revealed O isoconcentration surfaces at 4At.% O (Fig. 1b), as shown by atom probe tomography (APT). It clearly demonstrated that O was relatively uniformly dispersed throughout  $\alpha$  phases of the alloy, and its distribution exhibited a nanoscale LRO structure. We further analyzed the LRO-O structure by the average composition profile as a function of the distance to the iso-surfaces, which was calculated from one random LRO-O structure (Supplementary Fig. 2a inset). The resulting O profile is plotted in Supplementary Fig. 2a, b, along with the composition of the main constituents relative to their composition away from the structure, that is, in the  $\alpha$  phases, which reveals enrichment in O within the LRO-O structure. Moreover, the synchrotron X-ray diffraction (SXRD) analysis (Supplementary Fig. 3) rules out the presence of new metastable phases and another Ti-O oxide in the 0.36 O alloy, confirming the potential of LRO-O. Its formation originated from the second stage of the alloy preparation process; during this stage, multiple forging operations were performed in the  $\alpha + \beta$  phase region, followed by air cooling. With each reduction in the forging temperature, the enthalpy term in the Gibbs free energy becomes increasingly significant, leading to the formation of an LRO-O structure (including SRO-O and MRO-O) to minimize the free energy<sup>37</sup>. This structure represented a significant phenomenon in which no discernible O segregation was observed at phase or grain

boundaries and sharply contrasted with the typical interfacial O segregation reported in previous studies on Ti alloys, effectively preventing the degradation of mechanical properties commonly associated with interfacial brittleness. Furthermore, one-dimensional concentration profiles (Fig. 1c) revealed that the O concentration in the  $\alpha$  phase was markedly higher than that in the  $\beta$  phase. The LRO-O structures containing SRO-O structure (<1 nm) in the  $\alpha_s$  phase and MRO-O structure (>1 nm) in the  $\alpha_p$  phase were examined (Fig. 1d). Interestingly, the selected-area electron diffraction (SAED) patterns of the  $\alpha_s$  phase along the  $[2\bar{1}10]$  zone axis revealed additional diffuse disks (Fig. 1e). Although these disks exhibit noticeable broadening compared to those of a typical hexagonal close-packed (HCP) lattice, they remain discernible at intermediate positions, indicating the formation of an SRO-O structure in the  $\alpha_s$  phases. The high-angle annular bright field scanning transmission electron microscopy (HAABF-STEM) image (Fig. 1f) of the  $\alpha_s$  phase and intensity profile (Fig. 1g) further confirmed that O occupied the interstitial sites within the HCP lattice with comparable frequencies. Diffuse superlattice diffraction spots (Fig. 1e) can be visualized and their features entity further revealed through the central dark-field phase and a close-up view in the inset (Fig. 1h). The average size of the SRO-O entities identified is  $\bar{d} = 0.7$  nm (Fig. 1i). Interestingly, along the  $[2\bar{1}10]$  zone axis in the  $\alpha_p$  phase (Fig. 1j), diffuse scattering almost disappeared, shifting to additional spots of concentrated diffraction intensity, as shown by the arrows (one of which is circled in white); thus, the degree of LRO-O increased and provided strong evidence for the presence of MRO-O. Additionally, these diffraction spots were significantly weaker in intensity than the sharp spots from the HCP lattice of the  $\alpha_p$  phase. Similarly, O in the  $\alpha_p$  phase occupies the same interstitial sites within the HCP lattice with comparable frequencies (Fig. 1k). This difference in the LRO-O structures of the  $\alpha_p$  and  $\alpha_s$  phases could be related to their relative O content resulting from different formation condition. To observe the locations and dimensions of coherently diffracting regions, MRO-O entities were further observed in the central dark-field image and a close-up view in the inset (Fig. 1l). The vast majority (95%) of these MRO-O entities are approximately 1 nm in size, with an average size of  $\bar{d} = 1.6$  nm (Fig. 1m). These observations are consistent with the SAED patterns and central dark image in Supplementary Fig. 2c–f.

### Tensile and fatigue properties

The engineering stress–strain curves (Fig. 2a) show that 0.36 O alloy achieves an excellent combination of yield strength (1758 MPa) and ultimate tensile strength (1779 MPa), with a strain to failure of up to 7.9%. The magnification image of the tensile curve (inset of Fig. 2a) reveals a pronounced double-yielding phenomenon, which is distinct from conventional results. Compared to the 0.36 O alloy containing the LRO-O structure, the 0.22 O alloy exhibits lower yield strength (1641 MPa), ultimate tensile strength (1704 MPa), and strain to failure (4.8%). The distinction is also evident in the strain-hardening behavior after elastic deformation, characterized by a rapid marked rise (0.36 O alloy) and decline (0.22 O alloy) in the strain-hardening rate curves (Fig. 2b). This behavior of 0.36 O alloy indicates the activation of additional deformation mechanisms that contribute to the maintained ductility<sup>38</sup>. Previous studies on Ti alloys have consistently demonstrated that the soft phase ( $\alpha_p$ ) undergoes plastic deformation, the hard phase ( $\alpha_s$ ) remains in the elastic region, and the macroscopic yielding typically occurs after the hard-phase components<sup>39,40</sup>. Therefore, unlike traditional Ti alloys, our designed 0.36 O alloy exhibits different plastic deformation behavior, which occurs after  $\alpha_p$  phase plastic deformation and before  $\alpha_s$  phase plastic deformation and is related to the microstructures and presence of inner LRO-O structures. Most importantly, this 0.36 O alloy achieves an exceptional combination of yield strength and good ductility and surpasses other high-O and typical metastable  $\beta$  high-strength Ti alloys (Fig. 2c and Supplementary Note 1). The designed 0.36 O alloy retains an exceptional

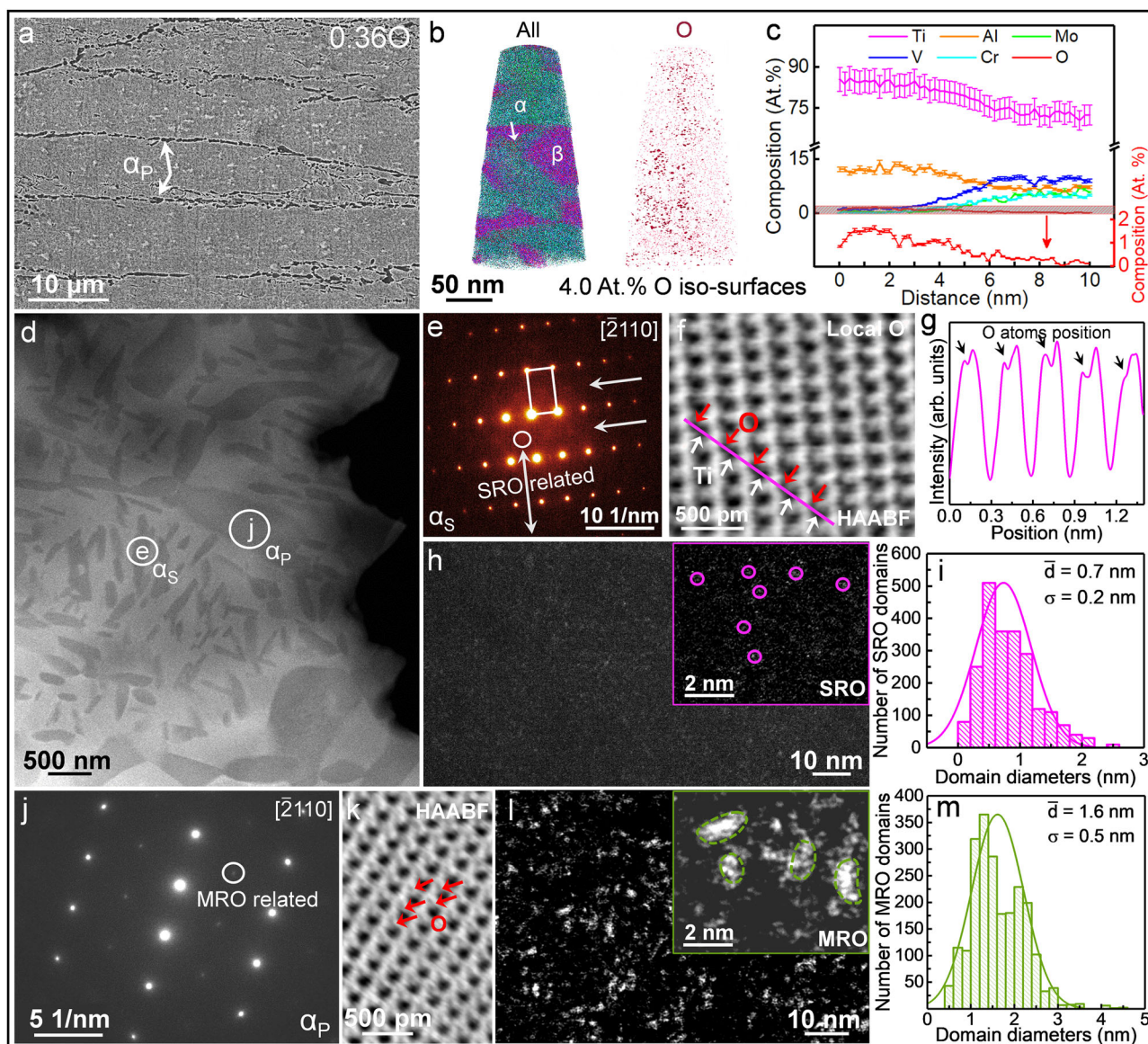


**Fig. 1 | Microstructure and characteristics of the local range order O structure (LRO-O, containing short/medium-range order O (SRO-O/MRO-O) in the 0.36 O alloy.** **a** Microstructure image of the designed alloy using scanning electron microscope (SEM). **b** Atom probe tomography (APT) three-dimensional reconstruction, showing the uniform dispersion of O and the absence of O segregation. Besides, the distribution maps of Ti, Al, Mo, V, and Cr elements are shown in Supplementary Fig. 4. **c** One-dimensional concentration profile across the phases interface from  $\alpha$  to  $\beta$  phase, indicating that Al and O are primarily distributed in the  $\alpha$  phase, whereas Mo, V, and Cr are concentrated in the  $\beta$  phase. The error bars represent the standard deviation of the mean. **d** Microstructure image of this designed alloy obtained by transmission electron microscopy (TEM). **e** Selected-area electron diffraction (SAED) pattern of the SRO-O structure along the  $[2110]$  zone axis in the  $\alpha_s$  phase (colours are applied to highlight the SRO structure). The dark-field image is pseudocoloured for better visibility. **f** High-angle annular bright

field scanning transmission electron microscopy (HAABF-STEM) image of  $\alpha_s$  phase in image (d), with red arrows indicating O atom columns and white arrows indicating Ti atom columns. **g** Intensity profile corresponding line of image (f). **h** Central dark-field image from superlattice diffraction shows distinguishable SRO-O domains. **i** Size distribution of the identified SRO-O domains according to the central dark-field image in image (h), with the average size ( $\bar{d}$ ) and standard deviation ( $\sigma$ ) provided in the inset box according to the three similar images. **j** SAED patterns of the MRO-O structure along the  $[2110]$  zone axis in the  $\alpha_p$  phase. **k** HAABF-STEM image of  $\alpha_p$  phase in image (d), with red arrows indicating O atom columns. **l** Central dark-field image obtained using extra reflections from image (j), illustrating MRO-O superlattice entities. **m** Size distribution of the MRO-O domains according to the central dark-field image in image (l), with the average size ( $\bar{d}$ ) and standard deviation ( $\sigma$ ) provided in the inset box according to the three similar images.

synergy of strength and ductility, and its excellent performance is attributed to the robust contribution of the LRO-O structure. The fracture surface and cross-section microstructure of the 0.36 O alloy (Supplementary Fig. 5a, b, d, e) exhibit mixed fracture morphologies; these morphologies are characterized by the presence of numerous dimples and cleavage fractures. Additionally, the crack propagation path reveals irregular and rough features, further highlighting the interactions between the cracks and some microstructures or special structures (Supplementary Fig. 5c). Nevertheless, the tensile fracture

of the 0.22 O alloy exhibits significant necking (Supplementary Fig. 6a, b), featuring dimples and localized cleavage fracture with a larger area.

Regarding the high-cycle fatigue (HCF) test of the 0.36 O alloy at a load ratio of  $R = 0.1$  (Fig. 2d), the scatter in the fatigue life, expressed in terms of maximum stress ( $\sigma_{\max}$ ) as a function of the number of cycles to failure ( $N_f$ ), is minimal. The fatigue strength of the 0.36 O alloy (1058.3 MPa) is significantly superior to that of conventionally reported metastable Ti alloys (Fig. 2e and Supplementary Note 2). In contrast, the fatigue strength of the 0.22 O alloy (900.0 MPa) without LRO-

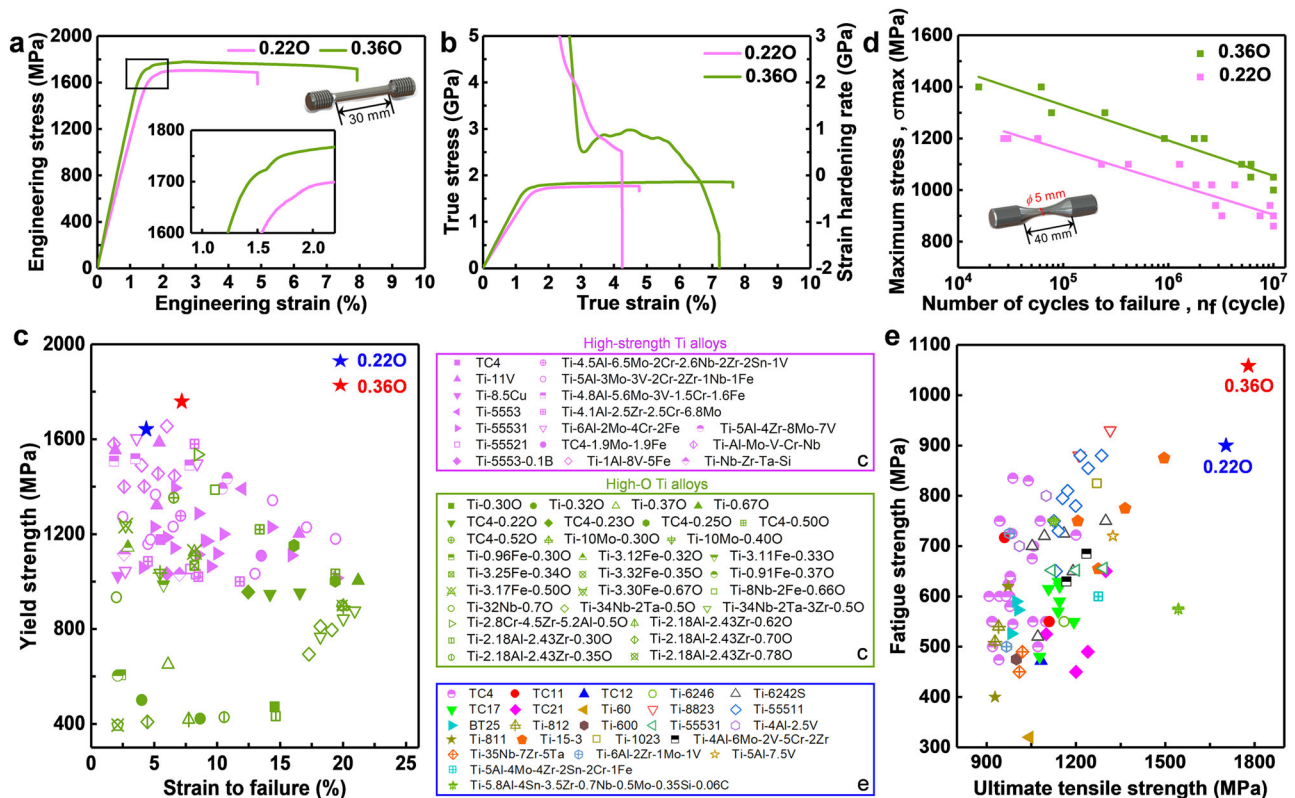


**Fig. 2 | Uniaxial tensile and high-cycle fatigue (HCF) performance of the 0.22 O and 0.36 O alloys.** **a** Engineering stress–strain curves, with the inset showing a magnified view of the double-yield stage and a schematic of the tensile test sample. **b** True stress–strain curves and their corresponding strain-hardening rate curves. **c** Comparison of the yield strength and fracture elongation for Ti and its alloys with high-O and typical high-strength Ti alloys. The corresponding literature sources are

detailed in Supplementary Note 1. **d** Maximum stress versus the number of cycles to failure (S–N) data at  $R = 0.1$ , and the inset illustrates a schematic of the HCF test sample. **e** Comparison of the ultimate tensile strength and fatigue strength among the different Ti alloys, the corresponding literature sources provided in Supplementary Note 2.

O structure is inferior to 0.36 O. The fracture morphology of the 0.36 O alloy exhibits a combination of dimples and cleavage features, with a rough fracture surface and irregular crack propagation paths (Supplementary Fig. 5f–n). These results indicate that the cracks originate from various sites, suggesting that fatigue cracks may randomly nucleate at stress concentrators or microstructural defects (Supplementary Fig. 5g, h). The irregular crack paths highlight the critical role of the microstructure in hindering fatigue crack propagation, indicating that crack growth is impeded by microstructural barriers such as grain boundaries, phase interfaces, or the LRO-O structure. The density of microcracks in 0.22 O alloy after fatigue fracture (Supplementary Fig. 6g, h) is significantly higher than that in the 0.36 O alloy, which is associated with several local stresses.

To comprehensively investigate the effects of the microstructure and the inner LRO-O structure on the mechanical properties of the 0.36 O alloy, in-situ tensile testing (Fig. 3) was conducted at both the macroscopic and microscopic scales using in-situ electron back-scattered diffraction (EBSD) and in-situ TEM, respectively. High-magnification in-situ scanning electron microscope (SEM) (Fig. 3a) observations were captured on the polished surface of the tensile specimen before tensile testing for comparison with the subsequent deformation stages. Based on the in-situ EBSD results at 5% strain (Fig. 3b), parallel slip lines were observed inside several  $\alpha_p$  phases, whereas cross-slip activity was also evident across many  $\alpha$  phase and  $\beta$  phase regions. As the strain increased to 10% (Fig. 3c), additional slip lines were detected within other  $\alpha_p$  grains, which attributed to the elevated tensile load exceeding the critical resolved shear stress of additional slip systems. Similarly, low-magnification images (Supplementary Fig. 7) and deformation information (Fig. 3d–f) were captured

and analyzed. In the macroscopic in-situ tensile tests, the engineering stress–strain curve (Fig. 3d and inset) exhibited a less pronounced double-yield phenomenon. The inverse pole figure (IPF) maps (Fig. 3(e1, f1)) showed significant lattice distortion, particularly at 10% strain. Compared with the kernel average misorientation (KAM) and grain orientation spread (GOS) results at 5% strain (Fig. 3(e2, e3)), 10% strain led to a marginal increase in local deformation and orientation shifts (Fig. 3(f2, f3)). These results were corroborated by an increase in the geometrically necessary dislocation (GND) density (Fig. 3(e4, f4)), which reached  $1.87 \times 10^{15} \text{ m}^{-2}$  at 10% strain. While the GND density increased as the strain increased from 5% to 10%, the KAM is anomalous correlation with GND, which was attributed to stress-relief mechanisms facilitated by multidirectional planar slip during the deformation process<sup>41</sup>. In this process, the LRO-O structure typically promoted a uniform dislocation distribution within grains. The activation of the cross-slip or multiple slip systems could locally increase the GND density due to strain incompatibility among the slip systems, without significantly altering the crystal orientation, thereby maintaining relative slightly KAM and GOS distributions. Therefore, the 0.36 O alloy exhibited exceptional deformation homogeneity and could withstand severe plastic deformation.

Furthermore, after elastic-plastic deformation of 0.36 O alloy samples without fracture and fracture failure, these deformation behaviors were observed using in-situ TEM by tensile test. In the former case, bundles of dislocations within  $\alpha_p$  phases were observed during the initial stages of loading, and these dislocations subsequently migrated within  $\alpha_p$  phases (Fig. 3g and Supplementary Movie 1). Rather than accumulating at the heterointerface, these dislocation bundles penetrated the  $\alpha_p$  phases, continued to propagate

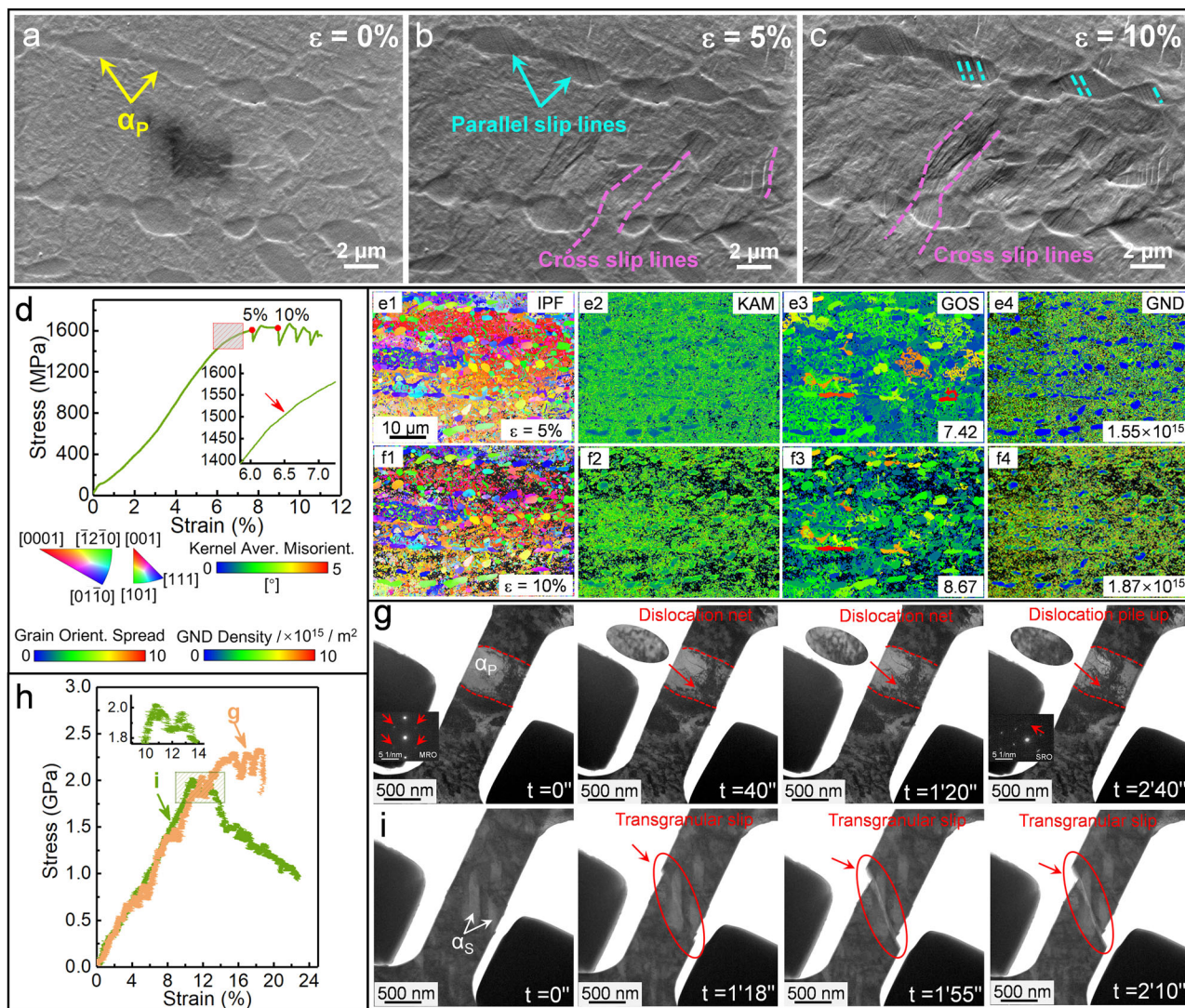


**Fig. 3 | In-situ tensile tests of the 0.36 O alloy at Room temperature.** **a–c** High-magnification in-situ SEM images of the tensile specimen at controlled strain levels of 0%, 5%, and 10%. The strains are not true engineering strains. **d** Stress–strain curves recorded during the in-situ electron backscattered diffraction (EBSD) process. **e** In-situ EBSD maps at 5% strain. **f** In-situ EBSD maps at 10% strain, respectively. The maps include the inverse pole figure (IPF) (**e1**, **f1**), kernel average misorientation (KAM, **e2**, **f2**), grain orientation spread (GOS, **e3**, **f3**), and geometrically necessary dislocation (GND, **e4**, **f4**). All samples were observed along the rolling direction from left to right. **g** Snapshot images from real-time in-situ tensile test

videos (Supplementary Movie 1) captured at different times. The sample was unloaded after plastic deformation without undergoing tensile fracture. The red dotted lines indicate the shape of the  $\alpha_P$  phase, and the SAED pattern images are shown in inset image obtained at the beginning and end of the test. **h** Stress–strain curves corresponding to the elastic-plastic deformation without fracture in image (**g**) and fracture failure in image (**i**). **i** Snapshot images from real-time in-situ tensile test video (Supplementary Movie 2) during tensile deformation. The area within the red solid line is where  $\alpha_S$  phases undergo transgranular slip. The tensile rate was maintained at 1 nm/s during the in-situ TEM tests.

into the interior, and formed localized dislocation networks during migration. Subsequently, local regions imposed a weaker barrier to dislocation motion, and led to a general reduction in the hindrance effect. Consequently, additional dislocations were continuously generated and migrated; thus, the alloy had excellent tensile ductility showing the platform from 15% to 19% strain (Fig. 3h, orange line). These results indicated that the dislocation in  $\alpha_P$  phases interacted with MRO-O structures, resulting in an SRO-O structure during tensile deformation, which were also demonstrated by the SAED patterns of  $\alpha_P$  (inset in the 0" and 2'40" capture images). Here, when the deformation ended, the diffuse spots of the MRO-O structure were no longer detected, and severe distortion of the lattice was observed by the deviating spots and the appearance of a ring structure.

The fracture failure sample exhibited exceptional tensile strength and ductility at room temperature before fracture, and its maximum elongation exceeded 20% (Fig. 3h, green line), which showed the

excellent tensile deformation capability of the alloy showing the strain-hardening at the 10%–14% strain first and then strain softening after the 14% strain. Snapshot images from real-time in-situ tensile testing of the 0.36 O sample were captured at various intervals (Supplementary Movie 2). When focusing on the  $\alpha_S$  phases, no significant dislocation motion was observed across the entire field of view. Instead, the transgranular slip happened, propagated from the lower right to the upper left of Fig. 3i, and involved two  $\alpha_S$  phases. Transgranular slip and multiple slip show obvious slip bands or local depressions on the macro level, and these deformations are relatively uniform (Supplementary Fig. 7). This phenomenon occurred because the deformed grains were influenced by the SRO-O structure, where the strain-hardening effect was pronounced. This increased the stress gradient between the adjacent grains, thereby promoting slip transmission. Further mechanisms for these dislocation phenomena are shown in Fig. 4.

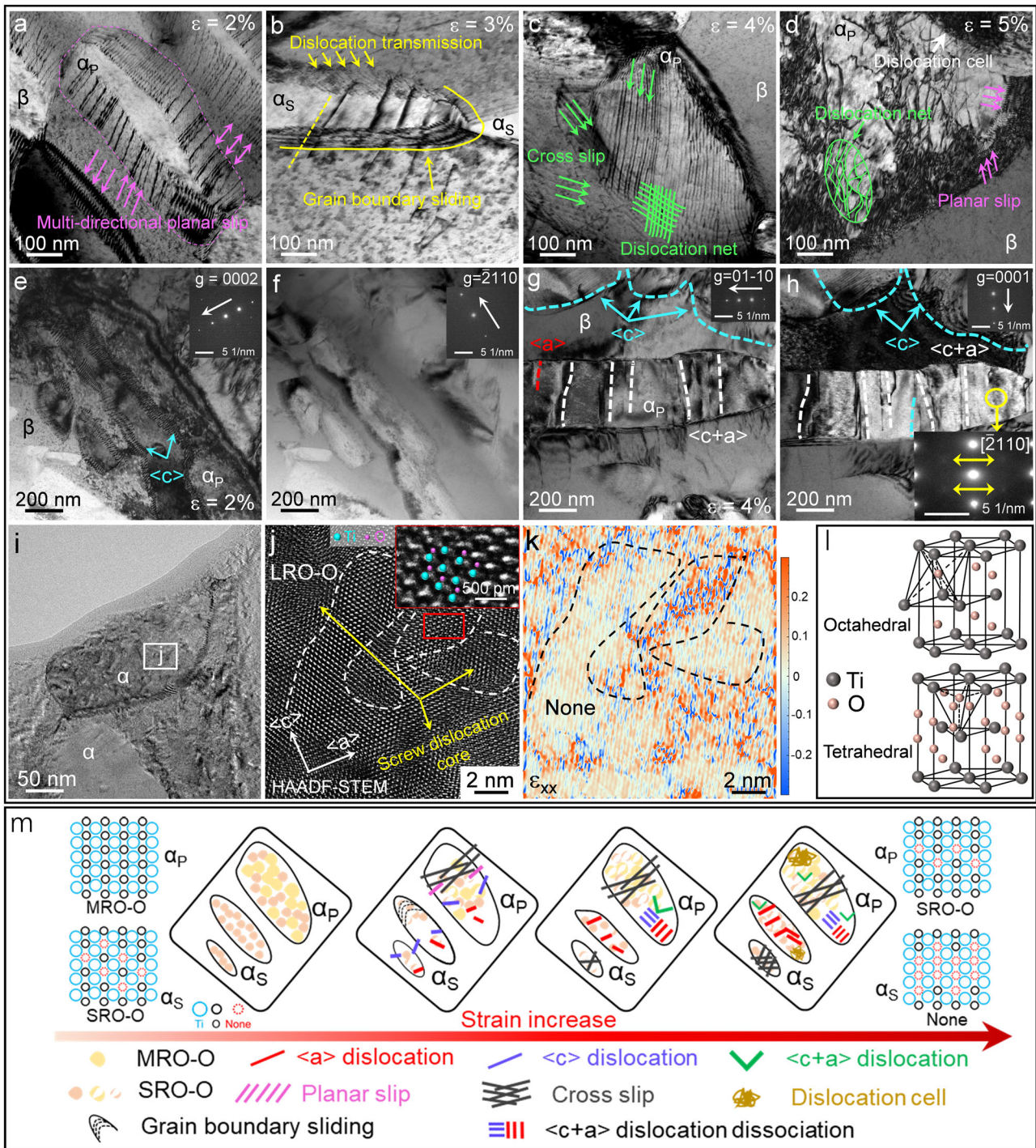


**Fig. 4 | Dislocation and interstitial O characteristics after tensile deformation of the 0.36 O alloy. a–d** Dislocation characteristics using ex-situ TEM at various strains of 2%, 3%, 4% and 5%. **e, f** Dislocation configurations at 2% strain in  $\alpha_p$  phase under  $g = [0002]$  and  $g = [-2110]$ . **g, h** Dislocation configurations at 4% strain in  $\alpha_p$  phase under  $g = [01-10]$  and  $g = [0001]$ . **i** Microstructure morphology. **j** High-angle annular dark field scanning transmission electron microscopy (HAADF-STEM) image corresponding in image (i) of  $\alpha$  phase. The top right corner shows a high-magnification HAADF-STEM image. **k** Corresponding geometrical phase analysis (GPA) for the stress distribution of image (j). **l** Diagram of the interstitial O atoms in the tetrahedral site and octahedral site. **m** Diagram of the LRO-O structure in a 0.36 O alloy and its effect and variation on tensile deformation.

image corresponding in image (i) of  $\alpha$  phase. The top right corner shows a high-magnification HAADF-STEM image. **k** Corresponding geometrical phase analysis (GPA) for the stress distribution of image (j). **l** Diagram of the interstitial O atoms in the tetrahedral site and octahedral site. **m** Diagram of the LRO-O structure in a 0.36 O alloy and its effect and variation on tensile deformation.

**Mechanism of strength–ductility–fatigue resistance matching**

The failure of the 0.22O alloy is attributed to deformation twinning and dislocation accumulation (Supplementary Fig. 8). Nanoscale twins (5–15 nm) initially formed to accommodate strain, while O strengthened the  $\alpha$  phase less effectively than in the 0.36 O alloy. Dislocation pile-ups at the  $\alpha/\beta$  interface caused local stress concentrations, leading to twin nucleation. As deformation progressed, twinning alone could

not sustain the increasing stress, resulting in intensified stress concentrations and the initiation of internal cracks, as evidenced by microcracks near the fracture surface and pronounced necking (Supplementary Fig. 6b).

Additionally, based on the above microstructural observations in 0.36 O alloy, the excellent mechanical properties were attributed to the unique characteristics of the designed LRO-O structure within the

$\alpha_S$  and  $\alpha_P$  phases combined with the dislocation interactions. The experimental evidence presented herein accentuated the significant strengthening and toughening effects imparted by the LRO-O structure and elucidated the intriguing phenomena of dislocation dissociation and motion in its presence. The dislocation behavior under various strain levels ranging from 2% to 5% was systematically investigated using ex-situ TEM (Fig. 4a–d). The TEM samples were extracted from equivalent positions within the deformed region to ensure consistency, since no fracture was observed in the specimens. Interestingly, at low strain levels, multidirectional planar dislocations slip within the  $\alpha_P$  and  $\beta$  phases (Fig. 4a), and grain boundary sliding, accompanied by this, was identified within the  $\alpha_S$  phase (Fig. 4b). In fact, these planar dislocations are likely to originate from the softer  $\beta$  phase, which is highly consistent with the in-situ TEM straining test observations—conducted on a sample taken from the center of the gauge section at 1% strain—where planar slip was found to traverse the  $\alpha/\beta$  interfaces and form a dislocation network within the  $\alpha_P$  phase (Supplementary Fig. 9, Supplementary Movie 3). At room temperature, grain boundary sliding was facilitated by the coordination of atomic-scale direct sliding and short-range atomic diffusion; this effectively mitigated crack formation and enabled substantial ductility<sup>42</sup>. At this stage, the alloy's plastic deformation was governed primarily by a multidirectional planar slip mechanism and characterized by a relatively uniform slip plane and minimal impediments to dislocation motion. Moreover, certain regions of the  $\alpha_S$  phase were already engaged in plastic deformation during the deformation initial stages and were the cause of the first yield phenomenon. Additionally, the transmission of dislocations from the  $\beta$  phase into the  $\alpha_P$  phase (Supplementary Fig. 9 and Supplementary Movie 3) also contributes to the initial yielding of the alloy. As the strain increased to 4%, cross-slip dislocations became evident (Fig. 4c), indicating a higher frequency of transitions between the slip planes within the material. By 5% strain (Fig. 4d), the dislocation motion encountered more obstacles, resulting in dislocation pile-ups. This accumulation contributed to an increase in material strength and was shown as plastic deformation accompanied by pronounced work hardening.

Interestingly, the  $\langle c \rangle$ -type dislocations were identified in the alloy designed for this study using dual-beam diffraction analysis (Fig. 4e–h). A significant proportion of these dislocations were screw types and were aligned parallel to the [0002] (Fig. 4e) and [0001] (Fig. 4h) directions. Compared with the  $\langle a \rangle$ -type and  $\langle c+a \rangle$ -type dislocations, the  $\langle c \rangle$ -type dislocations with a  $\langle 0001 \rangle$  Burgers vector were long considered energetically unstable and unlikely to self-nucleate within the HCP lattice during deformation<sup>43</sup>. The formation of the  $\langle c \rangle$ -type dislocations was usually driven by the localized decomposition of the  $\langle c+a \rangle$ -type dislocations into the  $\langle c \rangle$ -type and  $\langle a \rangle$ -type components<sup>44,45</sup>. In this study, the  $\langle c \rangle$ -type dislocations were observed at 2% strain, whereas all three dislocation types were detected at 4% strain in the alloy with the designed LRO-O structure, which indicated that the LRO-O structure had dual functionality. It facilitated the nucleation of the  $\langle c \rangle$ -type dislocations at lower strain levels (Fig. 4e) and promoted the dissociation of the  $\langle c+a \rangle$ -type dislocation into the  $\langle c \rangle$ -type and  $\langle a \rangle$ -type component at higher strains (Fig. 4g, h). The emergence of the  $\langle c+a \rangle$ -type dislocations at higher strains further indicated the activation of a more complex slip system within the material, and this behavior was closely associated with the strain-induced dislocation interactions<sup>46</sup>. The dislocation dissociation resulted in the decomposition of the original MRO-O structure within the  $\alpha_P$  phase into an SRO-O structure. This phenomenon was confirmed by the changes in the SAED pattern (Fig. 4h, inset) as well as by the central dark-field images and the size distribution of the SRO-O structures (Supplementary Fig. 10).

The LRO-O structure in the screw dislocation core was further analyzed using STEM images (Fig. 4i, j). O atom columns were observed at the HCP lattice tetrahedral sites on the tensile side of the

screw dislocation core (Fig. 4j and inset), whereas these columns were absent in the lower-stress regions without dislocations (Fig. 4k). Assuming that the stress state determined by in-situ EBSD (Fig. 3d–f) closely resembled the uniaxial tension applied to the specimen. The calculated Schmid factor (Supplementary Table 1) for  $(-1100) \langle 0001 \rangle$  slip (SF = 0.43) was comparable to that for the basal  $\langle a \rangle$  slip (SF = 0.44). This similarity suggested that the prismatic  $\langle c \rangle$  slip was relatively easy to activate in this material. When a  $\langle c \rangle$ -type dislocation nucleated on a prismatic plane, atomic shuffling along the normal direction of the prismatic plane (prismatic shuffling) became necessary<sup>47,48</sup>. In the presence of the O interstitial atoms located at the octahedral sites on the slip plane, the generalized stacking fault energy significantly increased. As slip progressed, the original octahedral positions on the slip plane gradually transformed into tetrahedral positions (Fig. 4l); this led to a reduction in the generalized stacking fault energy and the release of accumulated stress after severe deformation at high O concentrations<sup>49,50</sup>. This also explains that with the increase of strain, the dislocation density increases while the KAM and GOS change slightly. The interaction between the LRO-O structure and the core of  $\langle c \rangle$ -type screw dislocations was shown to manifest in phenomena such as the forced migration of O atoms from their original positions to the nearby  $\langle a \rangle$  planes, as well as the ability of O atoms near the dislocation core to induce partial cross-slip of dislocation lines onto the adjacent prismatic planes. These interactions were macroscopically manifested as a transgranular slip (Fig. 3 and Supplementary Fig. 7). Collectively, these effects resulted in a strong pinning effect on the screw dislocations, leading to significant strengthening. The activation of the prismatic  $\langle c \rangle$  slip increased the number of independent slip systems capable of accommodating external strain, which could be used to explain the enhanced ductility observed in the 0.36 O alloy (Fig. 4m). Evidently, the LRO-O structure played a critical role in the dislocation activation by reducing the energy barrier for the nucleation of the  $\langle c \rangle$ -type dislocations in the HCP lattice, and promoting the nucleation of additional dislocation types.

In this work, after the HCF test, the  $\langle c \rangle$ -type dislocations were detected within the unbroken 0.36 O alloy after  $10^7$  cycles (Fig. 5a, b), which is rarely observed. Research has shown that the  $\langle c \rangle$ -type dislocations in HCP structures can dissociate and facilitate the formation of twins<sup>51</sup>. When free  $\langle c \rangle$ -type dislocations interact with the  $\langle a \rangle$ -type dislocations within the same grain, they may collectively form twins through a classic “pole mechanism”<sup>52</sup>. Therefore, the HCF deformation behavior observed after the fracture failure of the 0.36 O alloy was characterized not only by multidirectional planar dislocation slip (Fig. 5c, d) and the formation of numerous stacking faults (Fig. 5e, f) but also by the distinct presence of nanotwins (Fig. 5g, h). This observation contrasted with typical uniaxial tensile deformation, where twin activity was significantly suppressed when the O content exceeded 0.2 wt%<sup>10,53</sup>. Furthermore, during HCF test, the cross-slip was notably inhibited in the  $\alpha$  phase, and the multidirectional the planar slip was enhanced and caused by the anisotropic stress distribution of the  $\alpha$  phase under alternating stress. It was driven by the LRO-O structure as shown in the twin and geometrical phase analysis (GPA) images (Fig. 5i–l). Within the  $\alpha$  phase, where the LRO-O structure in the crack (Fig. 5i inset) was nearly present, the stress concentration occurred in the regions containing the LRO-O structure post-fatigue, whereas areas devoid of O exhibited lower stress levels (Fig. 5k). Conversely, within the twins (Fig. 5m, n), the stress state in O-rich regions was lower than that in O-depleted areas (Fig. 5o, p), which indicated that the LRO-O structure maintained plastic deformation in localized regions while ensuring high strength. This occurred because the presence of the LRO-O structure effectively suppressed dislocation cross-slip during cyclic loading, and further promoted a transition from wavy to planar dislocation slip. This shift helped mitigate the surface deformation and the propagation of microcracks in the alloy

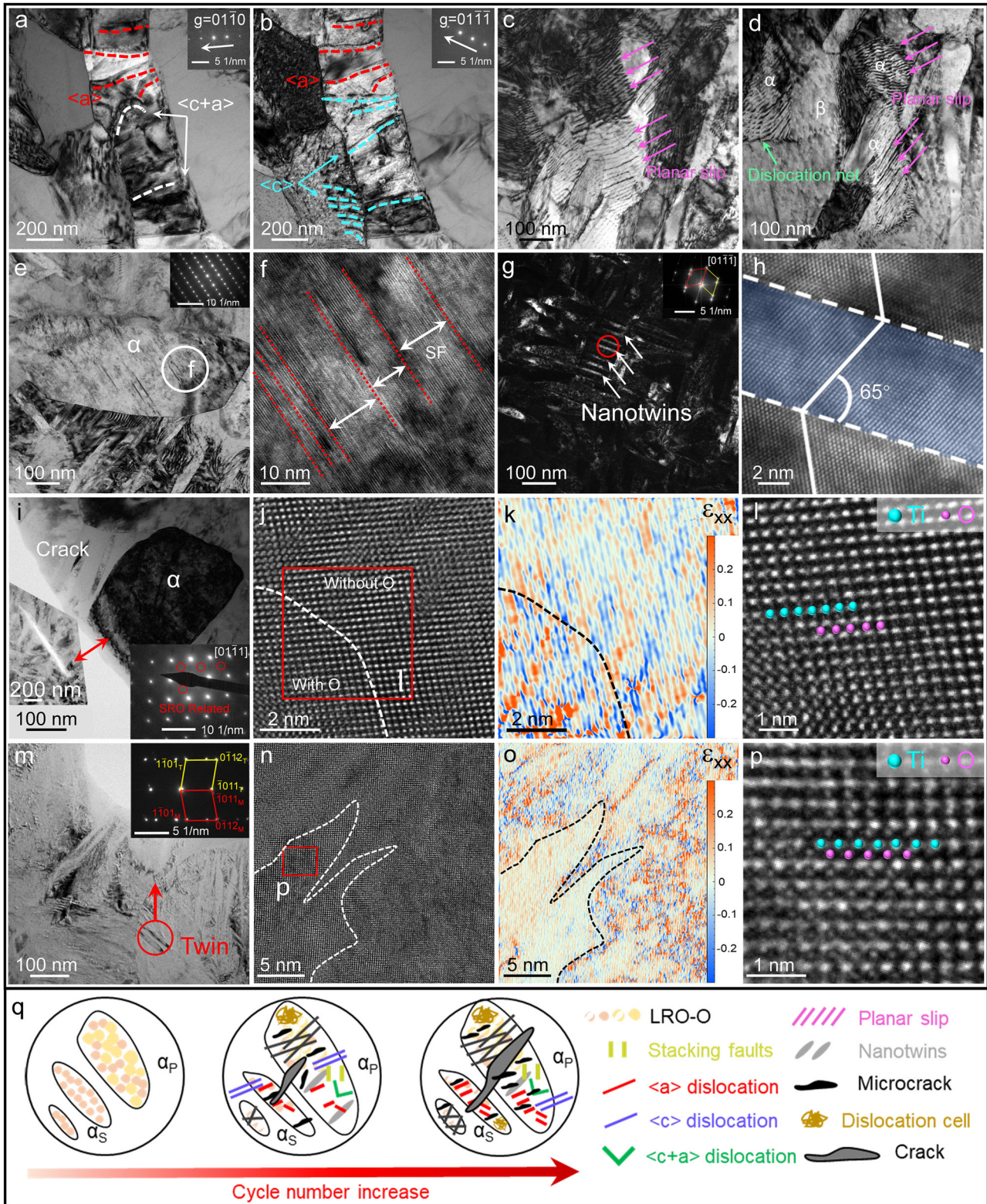


**Fig. 5 | Deformation characteristics after HCF fracture of the 0.36 O alloy.** **a, b** Dislocations of the  $\langle a \rangle$ -,  $\langle c \rangle$ - and  $\langle c + a \rangle$ -types observed on the unbroken sample after  $10^7$  cycles ( $\sigma_{\max} = 1050$  MPa,  $N_f = 10^7$ ) in the SAED patterns using  $g \cdot b = 0$ . **c, d** Planar slip morphology observed via TEM in the fracture failure sample ( $\sigma_{\max} = 1200$  MPa,  $N_f = 1.77 \times 10^6$ ). **e** Stacking faults within the  $\alpha$  phase observed in the fracture failure sample ( $\sigma_{\max} = 1200$  MPa,  $N_f = 1.77 \times 10^6$ ) and the inset image corresponding to its SAED pattern. **f** High resolution transmission electron microscopy (HRTEM) image of stacking faults. **g** Dark-field image of nanotwins with a twin angle of  $65^\circ$  on the fracture failure sample and inset image corresponding to its SAED pattern. **h** HRTEM image of nanotwins in image (g). **i** Microstructure in the

crack edge with the LRO-O structure confirmed by the inset SAED pattern. The inset low magnification image of the morphology on the left shows the crack. **j** HAADF-STEM image of the  $\alpha$  phase with the LRO-O structure in image (i). **k** Corresponding GPA on the stress distribution of image (j). **l** Magnified image of the LRO-O region in image (j). **m** Nanotwins in 0.36 O alloy after HCF fracture sample and its SAED in the inset image. **n** HAADF-STEM image of the nanotwins. **o** Corresponding GPA for the stress distribution of image (n). **p** Magnified image of the nanotwins and inner O atoms. **q** Diagram of the LRO-O structure in (a) 0.36 O alloy and its effect and variation on fatigue failure.

(Supplementary Fig. 5i–n). Moreover, the alternating distribution of the stacking fault widths significantly increased the difficulty of connecting partial dislocations. Thus, the conditions needed for dislocation cross-slip were impeded and crack initiation was blocked<sup>54</sup>. The relatively coarse internal structure (Supplementary Fig. 1h, i) was characterized by a disordered distribution and provided an increased capacity for dislocation accommodation. This increased capacity was effective in blunting crack tips and inhibiting crack propagation<sup>55</sup>. Therefore, the microstructure of the 0.36 O alloy was characterized by the LRO-O structure acting as a barrier and the interactions between the fatigue cracks and the barrier significantly decelerated the crack growth (Fig. 5q), thereby extending the fatigue life of the alloy. Nevertheless, the morphological heterogeneity of  $\alpha_5$  lamellae in the 0.22 O alloy induces localized strain incompatibility (Supplementary Fig. 1l), which severely impedes dislocation behavior due to the lack of LRO-O structures, although it activates alternative deformation pathways, such as twinning and stacking faults, ultimately resulting in a fatigue strength lower than that of the 0.36 O alloy. Further, the designed alloy of 0.36 O with LRO-O structures in this study exhibited excellent fatigue resistance and achieved superior strength-ductility synergy. The design paradigm presented here is applicable to a broad range of commercial Ti alloys, as well as high-entropy and Ni-based alloys, and can be readily scaled up to enhance the fatigue performance of large, complex structural components such as compressor blades.

## Methods

### Sample preparation

The Ti-5Al-5Mo-5V-3Cr-xO ( $x = 0.22$  wt% and 0.36 wt%) alloy in this study was synthesized via powder metallurgy approach from a powder mixture prepared. The powders are hydride-dehydrided Ti powder containing about 0.15 wt% and 0.3 wt% O, Al-Mo master alloy powders, pure V, and pure Cr powders (Supplementary Fig. 12a). The preparation process, thermomechanical treatment, and microstructural characteristics of the 0.22 O and 0.36 O alloys are discussed (Supplementary Fig. 12b). After vacuum sintering (1250 °C), the ingots (30 kg) underwent a three-stage thermomechanical process. The  $\beta$ -transition temperature of 0.22 O and 0.36 O alloys are  $945 \pm 5$  °C and  $975 \pm 5$  °C, respectively. First, the cogging was conducted in the  $\beta$ -phase region with a 630-ton forging press. In the second stage, forging was performed several times in the  $\alpha + \beta$  phase region, followed by air cooling. In the final stage, the alloy was rolled using a 550-ton horizontal bar mill in the  $\alpha + \beta$  phase region to obtain the alloy rods with a 16 mm diameter. Finally, the alloys were subjected to annealing at 550 °C for one hour using a conventional muffle furnace, followed by air cooling. In addition, the chemical composition of the 0.22 O and 0.36 O alloys were determined to be 5.11/5.03 Al, 5.08/5.12 Mo, 5.05/4.98 V, 3.13/3.06 Cr, 0.22/0.36 O, 0.08/0.09 Fe, and the balance Ti (wt%) using inductively coupled plasma mass spectrometry and Fusion Master ONH836 oxygen/nitrogen/hydrogen elemental analyzer.

### Mechanical tests

After heat treatment, the alloy billets were machined into smooth, standard tensile and fatigue specimens using electrical discharge machining. All specimens were polished using SiC paper, with grit sizes ranging from 400# to 2000#, and the polishing direction was aligned parallel to the loading direction. To ensure the reliability of the mechanical testing, a minimum of three tests were performed for each processing condition. Tensile tests were performed on a tensile machine (Zwick Roell Z100TWE) at ambient temperature under a tensile rate of 0.5 mm/min. The standard dimensions of the tensile specimens had a gauge length of 30 mm, a gauge section diameter of 5 mm, a threaded end diameter of 10 mm, and a total length of 64 mm. The schematic of the tensile sample is shown in Fig. 2a inset. These specimens were truncated from the bar parallel to the rolling direction.

The HCF tests were conducted at room temperature using an electrohydraulic servo fatigue testing system (Zwick HFP 5100), with a stress ratio  $R = 0.1$  and a frequency of 30 Hz. The tests were ended when the fatigue life reached  $10^7$  cycles without specimen failure. The specimens were 80 mm in length and 5 mm in gauge width and the schematic of this sample was shown in Fig. 2d inset. Due to the stringent surface roughness requirements for fatigue testing, minor surface defects from machining were removed to ensure accuracy.

### Microstructural characterization

**SEM.** The microstructure of the 0.22 O and 0.36 O alloys were examined using a SEM (Tescan Mira3).

**SXRD.** The SXRD experiments of 0.36 O alloy was performed at beamline ID31 of the European Synchrotron Radiation Facility. The wavelength of the X-ray was 0.16520 Å and the measured intensities were collected using a Pilatus CdTe 2M detector ( $1679 \times 1475$  pixels,  $172 \times 172 \mu\text{m}^2$  each). The distances from the sample to detector is approximately 1.5 m. The integration of the 2D XRD pattern was performed with the software pyFAI, followed by image integration, including flat-field, geometry, solid-angle, and polarization corrections.

**TEM and STEM.** Transmission electron microscopy (TEM, FEI Tecnai G2 F20) samples were mechanically thinned to 80  $\mu\text{m}$ , followed by electropolishing in a solution of 6% perchloric acid, 34% n-butyl alcohol, and 60% methanol at  $-20$  °C and 25 V. TEM observations were carried out at an accelerating voltage of 200 kV. Dark-field images were captured under various diffraction vectors ( $g$ ) in the dual-beam mode. The Burgers vector ( $b$ ) of dislocations was determined<sup>45</sup>. High-angle annular dark/bright field scanning transmission electron microscopy (HAADF/HAABF-STEM) was performed at 300 kV using double-aberration corrected microscopes for atomic resolution imaging (the TEAM 0.5), resulting from the transmission electron aberration-corrected microscope (TEAM, Titan Cubed Themis G2300). Drift correction was conducted with the methods developed by Ophus et al.<sup>56</sup> to eliminate artifact from the beam scan jittering. FRWR tools were used for the following GPA analysis. Averaged fast Fourier transforms were used as the strain templates.

**APT.** The distribution of O at the atomic scale across the  $\alpha/\beta$  phase interface and within both phases was examined using APT (Cameca LEAP 4000 HR). Specific APT samples from the targeted regions within the two phases were prepared using a focused ion beam (FIB, Helios G4 PFIB) and dual-beam SEM (FEI Helios Nanolab 600i). Needle-shaped APT samples were fabricated following the conventional lift-out technique using annular milling in dual-beam FIB instruments, either FEI Scios or FEI Helios 600i, as described in ref. 57. APT characterization was conducted using the local electrode atom probes LEAP 4000X HR and 5000XR (Cameca Instruments). The samples were analyzed in both voltage mode (pulse repetition rate of 200 kHz and pulse fraction of 0.2) and laser mode (pulse repetition rate of 250 kHz and pulse energy of 50 pJ). The specimen base temperature was maintained at 50 K, and the ion collection rate was set at either 0.5% or 1% per pulse. Three-dimensional reconstructions and data analysis were performed using the Interactive Visualization and Analysis Software (IVAS™), versions 3.6.14 and 3.8.

**In-situ EBSD test.** An in-situ tensile test was conducted using a tensile stage equipped with a 2 kN load cell within a SEM (JEOL 6100) featuring an AZtecHKL EBSD (EDAX Hikari Plus) system. The test employed a dog bone-shaped specimen with a thickness of 0.6 mm, a gauge length of 2 mm, and a gauge width of 1.8 mm. Both specimen faces were ground to a 4000-grit using SiC paper. Next, ion milling technology was used for surface treatment of the samples. This technique utilized an Ar ion beam to sputter the material's surface, effectively avoided

mechanical damage to the sample, and yielded high-quality samples with smooth surfaces. The ion milling process was conducted using a Leica EM TIC3X system, with the Ar ion beam energy set to 5 kV, a beam current of 1.5 mA, and a beam incidence angle of 6°. The milling duration was controlled at 60 min. The specimen was subjected to incremental loading at a displacement rate of 0.02 mm/min, and crosshead displacement was monitored via a linear variable differential transformer position transducer. To capture surface characteristics at specific deformation stages, the loading was paused at predetermined stress values, and crystallographic orientations were analyzed at each stop using EBSD. The SEM instrument was operated at 25 kV with a probe current of approximately 5 nA. Kikuchi diffraction patterns were recorded with 5 × 5 binning (128 × 96 pixels) and indexed using a standard Hough-transform-based automated procedure at a rate of 200 points per second. A step size of 0.4 μm was used for scanning, and each step needed approximately 60 min to complete. The acquired EBSD data were post-processed using AztecCrystal software.

**In-situ TEM tensile test.** The specimens were further reduced to a thickness of approximately 100 μm by gentle polishing using high grit emery paper. One end of each rectangular specimen was electrochemically polished to a thickness of 5–10 μm. Submicron sized pillars with dog-bone shapes were then fabricated using FIB machining following the procedure adopted by Liu et al.<sup>58</sup>. Extreme care was exercised to mitigate the damage due to gallium ions. The in-situ tensile test was conducted using a Hysitron PicoIndenter (PI95) within a Field Emission Gun (FEG) JEOL 2100F transmission electron microscopy (TEM) operating at 200 keV.

## Data availability

All the data supporting the results and findings of this study are provided in the paper and the Supplementary Materials. Source data are provided with this paper.

## References

- Zhang, Y. et al. Nacre-like surface nanolaminates enhance fatigue resistance of pure titanium. *Nat. Commun.* **15**, 6917 (2024).
- Choisez, L. et al. High temperature rise dominated cracking mechanisms in ultra-ductile and tough titanium alloy. *Nat. Commun.* **11**, 2110 (2020).
- Ritchie, R. O. The conflicts between strength and toughness. *Nat. Mater.* **10**, 817–822 (2011).
- Gao, J. et al. Deformation mechanisms in a metastable beta titanium twinning induced plasticity alloy with high yield strength and high strain hardening rate. *Acta Mater.* **152**, 301–314 (2018).
- Sun, F. et al. Investigation of early stage deformation mechanisms in a metastable β titanium alloy showing combined twinning-induced plasticity and transformation-induced plasticity effects. *Acta Mater.* **61**, 6406–6417 (2013).
- Zhang, C. L. et al. Achieving superior strength-ductility balance in a novel heterostructured strong metastable β-Ti alloy. *Int. J. Plast.* **147**, 103126 (2021).
- Zhao, Q. et al. High-strength titanium alloys for aerospace engineering applications: a review on melting-forging process. *Mater. Sci. Eng., A* **845**, 143260 (2022).
- Chou, K. & Marquis, E. A. Oxygen effects on ω and α phase transformations in a metastable β Ti-Nb alloy. *Acta Mater.* **181**, 367–376 (2019).
- Chou, K., Li, N. & Marquis, E. A. Enhanced work hardening from oxygen-stabilized ω precipitates in an aged metastable β Ti-Nb alloy. *Acta Mater.* **220**, 117302 (2021).
- Chong, Y. et al. Mechanistic basis of oxygen sensitivity in titanium. *Sci. Adv.* **6**, eabc4060 (2020).
- Chong, Y. et al. Elimination of oxygen sensitivity in α-titanium by substitutional alloying with Al. *Nat. Commun.* **12**, 6158 (2021).
- Zhou, X. et al. Formation and strengthening mechanism of ordered interstitial complexes in multi-principle element alloys. *Acta Mater.* **281**, 120364 (2024).
- Wang, X. & Han, W. Oxygen-gradient titanium with high strength, strain hardening and toughness. *Acta Mater.* **246**, 118674 (2023).
- Zhang, C. et al. Oxygen-dislocation interaction-mediated nanotwinned nanomartensites in ultra-strong and ductile titanium alloys. *Mater. Today* **75**, 85–96 (2024).
- Chong, Y. et al. Oxygen interstitials make metastable β titanium alloys strong and ductile. *Acta Mater.* **257**, 119165 (2023).
- Chong, Y. et al. Grain refinement in titanium prevents low temperature oxygen embrittlement. *Nat. Commun.* **14**, 404 (2023).
- Fu, Y. et al. Substantially strengthening a dual-phase titanium alloy by moderate oxygen doping. *Scr. Mater.* **226**, 115236 (2023).
- Morita, M., Suzuki, S., Kato, Y., Li, W. & Umezawa, O. Tensile deformation of texture-controlled titanium with high oxygen content at room temperature. *Mater. Sci. Eng., A* **793**, 139660 (2020).
- Li, H. F., Zhang, P., Wang, B. & Zhang, Z. F. Predictive fatigue crack growth law of high-strength steels. *J. Mater. Sci. Technol.* **100**, 46–50 (2022).
- Gao, Y. et al. Manipulating TWIP/TRIP via oxygen-doping to synergistically enhance strength and ductility of metastable beta titanium alloys. *J. Mater. Sci. Technol.* **215**, 58–70 (2025).
- Li, C. -y, Liu, C. -m, Lu, T., Guo, Y. -l & Liu, B. In-situ preparation of high oxygen content titanium via wire arc additive manufacturing with tunable mechanical properties. *Trans. Nonferrous Met. Soc. China* **34**, 171–183 (2024).
- Song, T. et al. Strong and ductile titanium-oxygen-iron alloys by additive manufacturing. *Nature* **618**, 63–68 (2023).
- Zhang, J. et al. Designing against phase and property heterogeneities in additively manufactured titanium alloys. *Nat. Commun.* **13**, 4660 (2022).
- Jia, M. T., Zhang, D. L., Gabbitas, B., Liang, J. M. & Kong, C. A novel Ti-6Al-4V alloy microstructure with very high strength and good ductility. *Scr. Mater.* **107**, 10–13 (2015).
- Zhang, H. et al. Making a low-cost duplex titanium alloy ultra-strong and ductile via interstitial solutes. *Acta Mater.* **241**, 118411 (2022).
- Devaraj, A. et al. A low-cost hierarchical nanostructured beta-titanium alloy with high strength. *Nat. Commun.* **7**, 11176 (2016).
- Worsnop, F. F. et al. The influence of alloying on slip intermittency and the implications for dwell fatigue in titanium. *Nat. Commun.* **13**, 5949 (2022).
- Wu, Y. et al. Effect of stress ratio on very high cycle fatigue properties of Ti-10V-2Fe-3Al alloy with duplex microstructure. *J. Mater. Sci. Technol.* **34**, 1189–1195 (2018).
- Li, H. et al. Uniting tensile ductility with ultrahigh strength via composition undulation. *Nature* **604**, 273–279 (2022).
- Liu, C. et al. Multi-dimensional study of the effect of early slip activity on fatigue crack initiation in a near-α titanium alloy. *Acta Mater.* **233**, 117967 (2022).
- Zhang, D. et al. Additive manufacturing of ultrafine-grained high-strength titanium alloys. *Nature* **576**, 91–95 (2019).
- Zhu, Y. & Wu, X. Heterostructured materials. *Prog. Mater. Sci.* **131**, 101019 (2023).
- Gao, B. et al. Ultrastrong low-carbon nanosteel produced by heterostructure and interstitial mediated warm rolling. *Sci. Adv.* **6**, eaba8169 (2020).
- Lei, Z. et al. Enhanced strength and ductility in a high-entropy alloy via ordered oxygen complexes. *Nature* **563**, 546–550 (2018).
- Zhang, R. et al. Short-range order and its impact on the CrCoNi medium-entropy alloy. *Nature* **581**, 283–287 (2020).

36. Zhang, Y. J., Han, D. & Li, X. W. Improving the stress-controlled fatigue life of low solid-solution hardening Ni-Cr alloys by enhancing short range ordering degree. *Int. J. Fatigue* **149**, 106266 (2021).
37. Han, Y. et al. Ubiquitous short-range order in multi-principal element alloys. *Nat. Commun.* **15**, 6486 (2024).
38. Zhao, S. et al. Cryoforged nanotwinned titanium with ultrahigh strength and ductility. *Science* **373**, 1363–1368 (2021).
39. Huang, C. X. et al. Interface affected zone for optimal strength and ductility in heterogeneous laminate. *Mater. Today* **21**, 713–719 (2018).
40. Yang, M. et al. Residual stress provides significant strengthening and ductility in gradient structured materials. *Mater. Res. Lett.* **7**, 433–438 (2019).
41. Wang, L. et al. Tailoring planar slip to achieve pure metal-like ductility in body-centred-cubic multi-principal element alloys. *Nat. Mater.* **22**, 950–957 (2023).
42. Wang, L. et al. Tracking the sliding of grain boundaries at the atomic scale. *Science* **375**, 1261–1265 (2022).
43. Maldar, A. et al. Activation of <c> dislocations in Mg with solute Y. *J. Magnes. Alloy.* **12**, 1045–1053 (2024).
44. Wu, Z. & Curtin, W. A. The origins of high hardening and low ductility in magnesium. *Nature* **526**, 62–67 (2015).
45. Wei, K. et al. Grain size effect on tensile properties and slip systems of pure magnesium. *Acta Mater.* **206**, 116604 (2021).
46. Li, H., Mason, D. E., Bieler, T. R., Boehlert, C. J. & Crimp, M. A. Methodology for estimating the critical resolved shear stress ratios of  $\alpha$ -phase Ti using EBSD-based trace analysis. *Acta Mater.* **61**, 7555–7567 (2013).
47. Fan, H. et al. Core structures and mobility of <c> dislocations in magnesium. *Scr. Mater.* **135**, 37–40 (2017).
48. Dong, Q. et al. Basal-plane stacking-fault energies of Mg alloys: a first-principles study of metallic alloying effects. *J. Mater. Sci. Technol.* **34**, 1773–1780 (2018).
49. Yu, Q. et al. Origin of dramatic oxygen solute strengthening effect in titanium. *Science* **347**, 635–639 (2015).
50. Liu, C. et al. Direct observation of oxygen atoms taking tetrahedral interstitial sites in medium-entropy body-centered-cubic solutions. *Adv. Mater.* **35**, 2209941 (2023).
51. Ghazisaeidi, M. & Curtin, W. A. Analysis of dissociation of <c> and <a> dislocations to nucleate (10-12) twins in Mg. *Modell. Simul. Mater. Sci. Eng.* **21**, 055007 (2013).
52. Christian, J. W. & Mahajan, S. Deformation twinning. *Prog. Mater. Sci.* **39**, 1–157 (1995).
53. Hooshmand, M. S., Niu, C., Trinkle, D. R. & Ghazisaeidi, M. First-principles prediction of oxygen diffusivity near the (101-2) twin boundary in titanium. *Acta Mater.* **156**, 11–19 (2018).
54. An, X. H., Wu, S. D., Wang, Z. G. & Zhang, Z. F. Significance of stacking fault energy in bulk nanostructured materials: insights from Cu and its binary alloys as model systems. *Prog. Mater. Sci.* **101**, 1–45 (2019).
55. Fang, T. H., Li, W. L., Tao, N. R. & Lu, K. Revealing extraordinary intrinsic tensile plasticity in gradient nano-grained copper. *Science* **331**, 1587–1590 (2011).
56. Ophus, C., Ciston, J. & Nelson, C. T. Correcting nonlinear drift distortion of scanning probe and scanning transmission electron microscopies from image pairs with orthogonal scan directions. *Ultramicroscopy* **162**, 1–9 (2016).
57. Miller, M. K. & Russell, K. F. Atom probe specimen preparation with a dual beam SEM/FIB miller. *Ultramicroscopy* **107**, 761–766 (2007).
58. Liu, B. et al. Twinning-like lattice reorientation without a crystallographic twinning plane. *Nat. Commun.* **5**, 3297 (2014).

## Acknowledgements

This work was supported by the National Natural Science Foundation of China (Grant Nos. 52371092) and the National Key Research and Development Program of China (Grant Nos. 2022YFB3705605). We would thank P. Zhang at Xi'an Jiaotong University for microstructural characterization of materials in in-situ TEM tensile.

## Author contributions

Q.Y.Z. and Y.Q.Z. conceived the research. Y.M.M. conducted the experiments under the supervision of R.Q.Z., P.G., and Y.N.C. Y.M.M. analyzed and interpreted the data, and wrote the manuscript with input from Q.Y.Z. and Y.Q.Z. All authors contributed to the discussion.

## Competing interests

The authors declare no competing interests.

## Additional information

**Supplementary information** The online version contains supplementary material available at <https://doi.org/10.1038/s41467-025-62646-5>.

**Correspondence** and requests for materials should be addressed to Qinyang Zhao or Yongnan Chen.

**Peer review information** *Nature Communications* thanks Damon Kent and the other, anonymous, reviewer(s) for their contribution to the peer review of this work. A peer review file is available.

**Reprints and permissions information** is available at <http://www.nature.com/reprints>

**Publisher's note** Springer Nature remains neutral with regard to jurisdictional claims in published maps and institutional affiliations.

**Open Access** This article is licensed under a Creative Commons Attribution-NonCommercial-NoDerivatives 4.0 International License, which permits any non-commercial use, sharing, distribution and reproduction in any medium or format, as long as you give appropriate credit to the original author(s) and the source, provide a link to the Creative Commons licence, and indicate if you modified the licensed material. You do not have permission under this licence to share adapted material derived from this article or parts of it. The images or other third party material in this article are included in the article's Creative Commons licence, unless indicated otherwise in a credit line to the material. If material is not included in the article's Creative Commons licence and your intended use is not permitted by statutory regulation or exceeds the permitted use, you will need to obtain permission directly from the copyright holder. To view a copy of this licence, visit <http://creativecommons.org/licenses/by-nc-nd/4.0/>.

© The Author(s) 2025